Università degli studi di Padova

Dipartimento di Fisica e Astronomia "Galileo Galilei"

Master Degree in Astrophysics and Cosmology

FINAL DISSERTATION

Black hole - Wolf-Rayet binaries as progenitors of binary black holes

Candidate:
Erika Korb

Supervisor:
Prof. Michela Mapelli

Co-supervisor:
Dr. Giuliano Iorio

Academic Year 2021–2022

Abstract

I study the formation of binary black hole systems by means of population-synthesis simulations, with the code SEVN (Stellar EVolution for N-body). My main goal is to determine their formation history, with particular attention to mass transfer processes (stellar winds, Roche Lobe overflow, common envelope). I focus my work on the formation channels that include the production of a Wolf-Rayet - black hole binary, finding that this is the most common formation pathway at solar metallicity. I compare my results with the properties of the observed Wolf-Rayet - black hole systems, including the Cyg X-3 binary.

Contents

Chapter 1

Demography of the black hole binaries

In September 2015, the detection of the first gravitational wave GW150914 not only confirmed the existence of binary systems made of two stellar black holes but also demonstrated that such systems are capable of merging via emission of gravitational waves within a Hubble time H_0. [1] In March 2020, the LIGO Scientific, Virgo and KAGRA Collaboration ended the third observing run and, by November 2021, produced the third Gravitational-Wave Transient Catalog GWTC-3, revealing a total of ~ 80 merging binary black holes discovered with the gravitational wave detectors. Overall, the GWTC-3 revealed ~ 90 mergers of compact objects binaries, including also double neutron star and neutron star-black hole systems that won't be considered in this thesis. [2]

The formation pathaways of the black hole binaries are an active field of research and can be divided into two main evolutionary scenarios: isolated binary or dynamically active environments. Different formation histories can be investigated mainly by the analysis of the features in the distribution of the masses, spins and related quantities: different formation channels lead to different predictions on the black hole masses, mass ratio $q = M_2/M_1$ ($M_1 \geq M_2$), spin alignment and magnitude.

On the one hand, the isolated binary evolution assumes that tidal interactions and mass transfer episodes are so efficient to produce compact objects with similar masses, i. e. $q \sim 1$ [3] with spins aligned and parallel to the orbital angular momentum [4]. On the other hand

1.1 Gravitational waves observations

1.1.1 Theory and methods for parameter estimation

A match-filtering method   The detection and characterization of the binaries observed with the gravitational waves relies on matched-filtering techniques and Bayesian analysis.

First, the signal is detected with the match-filtering technique. The detection pipeline filters the recorded signal with waveform templates generated by numerical relativity calculations. Different binary properties produce different waveforms, therefore a match in the signal not only reveals a detection but allows an approximate estimate of the main binary parameters (masses, orbital separation, etc.).

Once the signal is detected, general-relativity models that include, for instance, spin precession are used to refine the waveform template and the fit. Eventually, Bayesian anaylsis is carried out to each model to derive posterior distributions of the source parameters: the final best estimates are usually the median values of the posterior with uncertainty given by the 90% credible interval extrema.

Spin determination   A black hole binary undergoing a quasi-circular inspiral is characterized by fifteen parameters: eight intrinsic (mass M_i and three-dimensional components of the spin vectors $\vec{S}_i$ for each i-th black hole) and seven extrinsic, for the sky location and orbit orientation (right ascension α, declination δ, luminosity distance d_L, orbital inclination ι, polarization angle Φ, time of coalescence t_c and phase at the coalescence ϕ_c). [5]

In reality, the three spin vectors are the most difficult parameters to characterize because they imprint a second-order effect in the waveform, requiring advanced numerical relativity calculations
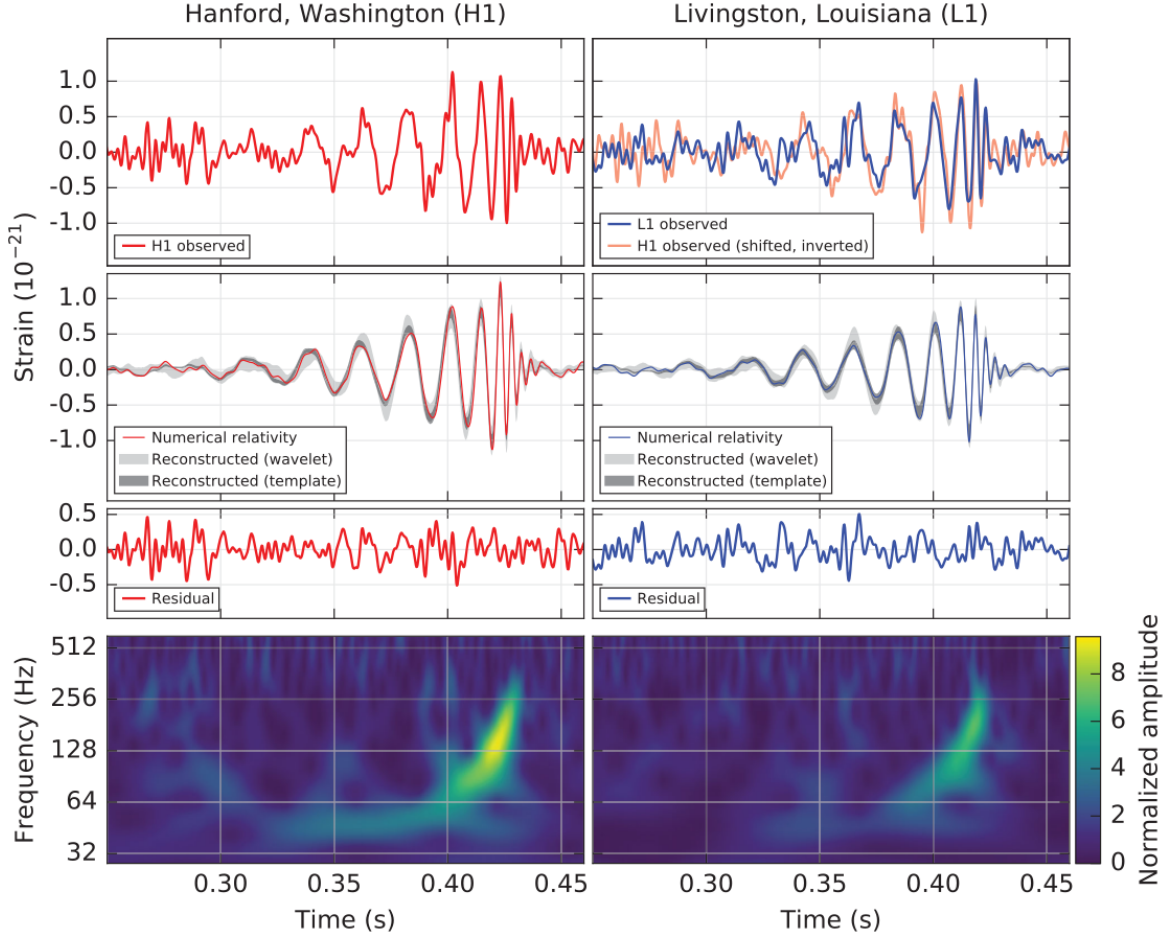
1

Figure 1.1: Signal detection of GW150914. *Top:* amplitude time-series. *Bottom:* frequency time-series. [1]

to be correctly modeled. In place of the six spin vectors, the pipeline anaylsis fits six effective spin parameters that are slightly easier to obtain from the observations: the two dimensionless spin magnitudes χ_i, the two polar tilt angles θ_i, the effective spin χ_{eff} and the effective precessing spin χ_p. All the values are calculated at the reference frequency of 20 Hz.

The *dimensionless spin* χ_i quantifies the amplitude of the spin by measuring how much the black hole is close to being a Schwarzschild, non-rotating black hole ($\chi_i = 0$) or to a maximally-spinning Kerr black hole ($\chi_i = 1$)

$$\chi_i = \frac{|\vec{S}_i|c}{GM_i} \quad \in [0,1] \qquad i = 1,2 \tag{1.1}$$

The *effective spin* χ_{eff} measures the mass-weighted component of the black hole spins that is aligned with the Newtonian orbital angular momentum $\hat{L}_N$ (normal to the orbital plane)

$$\chi_{eff} = \frac{(M_1\vec{\chi}_1 + M_2\vec{\chi}_2) \cdot \hat{L}_N}{M_1 + M_2} \tag{1.2}$$

The two polar angles θ_i measure the inclination of each black hole spin with respect to the orbital angular momentum $\hat{L}_N$. They enter in the definition of the *effective precessing spin*, which measures the dominant spin projected on the orbital plane, that eventually causes the relativistic precession of the orbital plane itself

$$\chi_p = \max\left\{\chi_1 \sin\theta_1, \ \left(\frac{3+4q}{4+3q}\right) q\chi_2 \sin\theta_2\right\} \tag{1.3}$$

where $q = M_2/M_1$ is the binary mass ratio. [6]

A toy model for the main parameter estimation   Beside the Bayesian analysis, it is still possible to obtain order-of-magnitude estimates of the key quantities that shape the waveform, like the orbital separations and the masses, by simply using as toy model a circular binary that converts all the orbital energy lost into gravitational wave radiation.

According to the theory of the general relativity, the amplitude of the gravitational wave is proportional to the second derivative with respect to time of the mass quadrupole moment of the compact source. Explicit calculation of the quadrupole moment of a circular binary relates the amplitude h of the gravitational wave emitted to the luminosity distance d_L, the gravitational wave frequency ν_{GW} and the chirp mass $\mathcal{M}$ according to

$$h = \frac{4}{d_L} \left(\frac{G\mathcal{M}}{c^2} \right)^{5/3} \left(\frac{\pi \nu_{\mathrm{GW}}}{c} \right)^{2/3} \tag{1.4}$$

where G is the gravitational constant and c the speed of light. [7, 8]

The *chirp mass* $\mathcal{M}$ is defined as a combination of the masses of the binary and is defined in every time interval of the signal by the different values ν_{GW} and slopes $\dot{\nu}_{\mathrm{GW}}$ of the gravitational wave frequency, as follows

$$\mathcal{M} = \frac{(M_1 M_2)^{3/5}}{(M_1 + M_2)^{1/5}} = \frac{c^3}{G} \left(\frac{5}{96} \, \pi^{-8/3} \, \nu_{\mathrm{GW}}^{-11/3} \, \dot{\nu}_{\mathrm{GW}} \right)^{3/5} \tag{1.5}$$

The chirp mass is easily obtainable from the signal analysis by Fourier-transforming the recorded amplitude time-series into a frequency time-series, as shown in Fig. 1.1. By re-arranging the definition of the chirp mass, it is possible to show that knowing the chirp mass puts a lower limit to the total mass of the system

$$(M_1 + M_2)_{\mathrm{min}} = 4^{3/5} \mathcal{M} \sim 2.3 \, \mathcal{M} \tag{1.6}$$

The gravitational wave frequency dependence in Eq. 1.4 already encloses all the information on the compactness of the orbit. The binary considered in the toy model is circular so its mass quadrupole moment is symmetric under a 180° rotation: every half-orbit the gravitational wave produced has the same phase. In other words, a circular binary produces a gravitational wave with frequency that is twice the rotational frequency: $\nu_{\mathrm{GW}} = 2\nu_{\mathrm{s}}$.

As the binary spirals-in, the orbit tightens and the rotational frequency increases, causing a rise also in the gravitational wave frequency and in the amplitude of the signal, according to Eq. 1.4: it is the so-called *chirp signal*. The peak of the signal, both in terms of frequency and amplitude, is reached at the coalescence, when the orbital separation reaches its minimum and is just the sum of the two Schwarzschild radii

$$R_{\mathrm{coalescence}} = \frac{2G}{c^2}(M_1 + M_2) \tag{1.7}$$

Using Kepler's third law and the relation $\nu_{\mathrm{GW}} = 2\nu_{\mathrm{s}}$, the peak frequency of the gravitational wave $\nu_{\mathrm{GW,peak}}$ can be related to the total mass of the binary by

$$\nu_{\mathrm{GW,max}} = \frac{1}{\pi\sqrt{8}} \frac{c^3}{G(M_1 + M_2)} \tag{1.8}$$

Coalescence to determine masses, orbital separation and luminosity distance   The coalescence is the key observational moment that allows to characterize the main parameters of the binary. Eq. 1.8 and 1.5 show that precise measurements on the peak frequency provide both the total and chirp mass of the system, allowing the disentanglement of the single masses. Measuring the peak frequency, therefore the total mass, also allows the determination of the orbital distance at coalescence. Given that the amplitude of the gravitational wave is directly the signal recorded by the detectors, it is possible to use Eq. 1.4 with the values known at the coalescence to obtain the luminosity distance of the source.

On the one hand, assuming a cosmological model, it is possible to convert the luminosity distance into the redshift of the source. On the other hand, gravitational wave observations provide an independent luminosity distance measurement that, coupled with electromagnatic counterpart observations, allow an independent method to estimate the Hubble cosmological parameter H_0. [9]
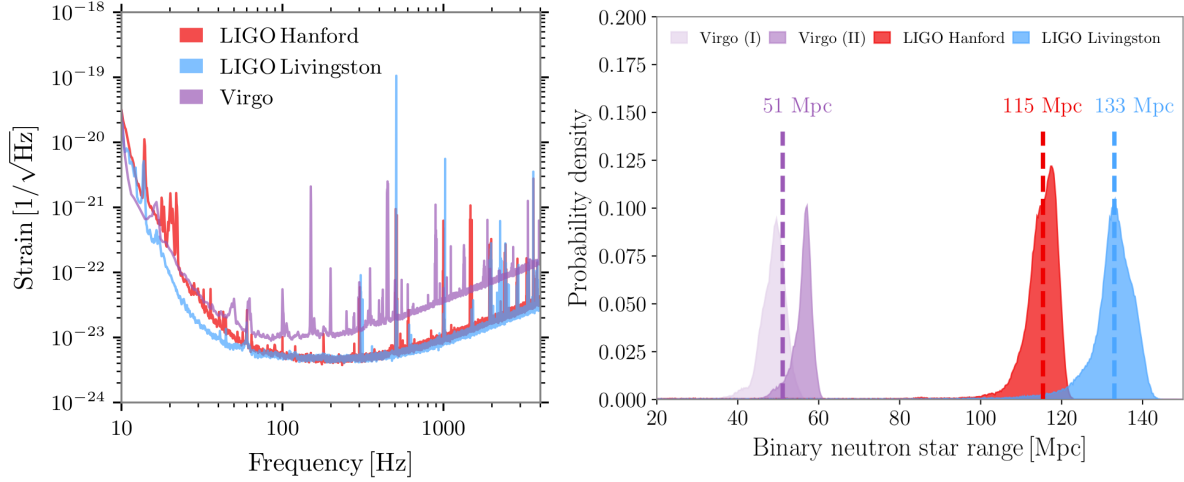
Figure 1.2: Sensitivity curves (*left*) and binary neutron star observational probability density (*right*) of the LIGO and Virgo interferometers during the third observing run O3. The lower sensitivity of Virgo for $\nu \gtrsim 150$ Hz limits the observable volume, especially for the lighter sources like the binaries of neutron stars. [2]

The gravitational waves are stretched by the expansion of the universe, therefore it is mandatory to use the redshift information to correct the parameters determined so far in the detector's frame and obtain the intrinsic ones in the source's frame. Because of the cosmological redshift z, the observed frequency of the gravitational wave is lower than the one emitted. The frequency-dependence enters in the determination of the chirp mass in Eq. 1.5 and, according to Eq. 1.8, a lower peak frequency results in an over-estimation of the source total mass. Eventually, both masses need to be reduced as

$$M_i^{source} = \frac{M_i^{det}}{(1+z)} \qquad i = 1, 2 \qquad (1.9)$$

GW150914-like binaries   It is possible to apply the above formulas to get an order-of-magnitude estimate of any binary detection. For instance, the Bayesian analysis of the signal of GW150914 reported in Fig. 1.1 revealed two black holes of masses $M_1 = 35.6^{+4.7}_{-3.1}\ M_\odot$ and $M_2 = 30.6^{+3.0}_{-4.4}\ M_\odot$ at redshift $z = 0.09^{+0.03}_{0.03}$ within 90% confidence intervals. [5] Using Eq. 1.9, the masses revealed in the detector frame where about 10% heavier, respectively $M_1 \sim 39\ M_\odot$ and $M_1 \sim 33\ M_\odot$. The corresponding chirp mass was $\mathcal{M} \sim 30 M_\odot$ and the total mass $M \sim 70\ M_\odot$, meaning that at the coalescence the binary had a radius of only $R_{\text{coalescence}} \sim 200$ km and produced a peak gravitational wave at $\nu_{\text{GW,peak}} \sim 300$ Hz. The binary had a luminosity distance of $d_L = 410$ Mpc and the gravitational wave was detected with an amplitude of $h \sim 10^{-21}$ Hz$^{-1/2}$.

Sensitivity, biases and future perspectives   According to Eq. 1.4, the further the sources and the lower the amplitude of the gravitational wave that reaches the detector. To have a quantitative comparison it is useful to use as proxy-source a binary neutron star: the limits on its equation of state impose that a single neutron star has at maximum a mass of $\sim 3\ M_\odot$, therefore the binary chirp mass is well-defined and doesn't exceed $\mathcal{M} \sim 2.6\ M_\odot$. [11] Fig. 1.2 reports the sensitivity curves of the LIGO and Virgo interferometers and the end of the third observing run O3, highlighting how the worst sensitivity of Virgo at the high frequency (mainly caused by the photon shot noise) limits the maximum observable distance of the binary neutron star by a factor of 2 when compared to the performances of LIGO. [2]

In terms of binary black holes, a source like GW150914 that peaks at $\nu \sim 300$ Hz could be observed by the LIGO interferometers with sensitivity of $h \sim 10^{-23}$ Hz$^{-1/2}$ up to a luminosity distance of $d_L \sim 1.6$ Gpc: the binary can now be observed in a volume of space ~ 64 times bigger. The observable volume is maximum for binaries that merge close to the best sensitivity range at $\sim 100-200$ Hz, that, according to Eq. 1.8 are likely binaries composed of heavy black holes with total mass of $M \sim 100-200\ M_\odot$: the gravitational wave detectors are biased towards the observation of heavy binary black holes.
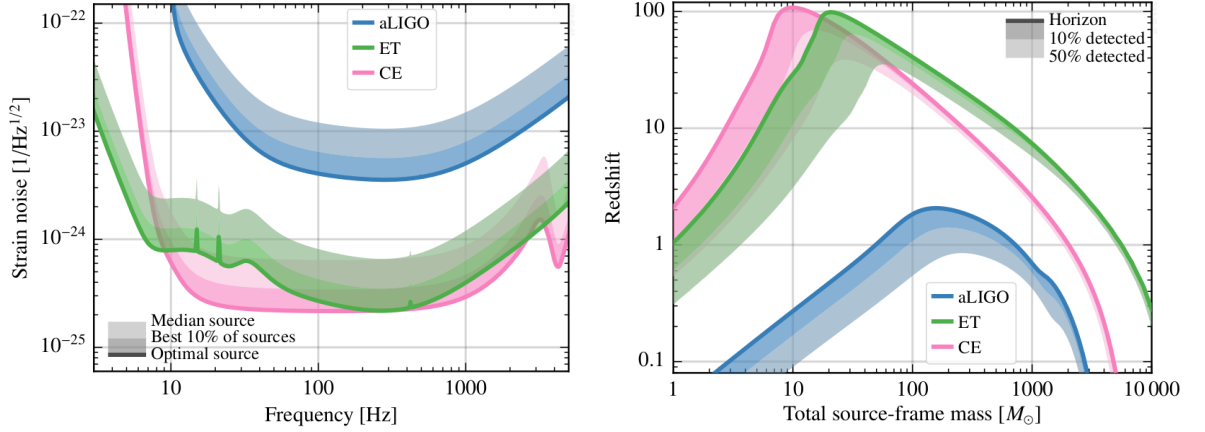
Figure 1.3: Example of the possible sensitivity curves (*left*) and observable horizons (*right*) of the planned third generation interferometers Einstein Telescope and Cosmic Explorer. Unlike the advanced LIGO interferometer, Einstein Telescope and Cosmic Explorer will detect for the first time black hole binaries well-beyond redshift $z \gtrsim 1$. [10]

Third generation gravitational wave detectors, like the planned Einstein Telescope and Cosmic Explorer, will be at least an order of magnitude more sensible than the refined versions of the LIGO and Virgo interferometers, allowing to probe the mergers of binary compact objects beyond redshift $z \gtrsim 1$. As shown in Fig. 1.3, the maximum observable distance depends on the source mass and on the interferometers sensitivity, that ultimately depends on its design and is still under development (Fig. 1.3 is only one of the proposed designs, but is representative of the goals of the projects). [10] Again, Eq. 1.4 underlines how the detection improvement is mainly for the black hole binaries: their heavier mass produces stronger amplitude signals than the neutron star binaries, making them visible even at cosmic distances.

1.1.2 Mass and spin observed distributions

Merger rate densities and posterior distribution The parameter distributions of the observed gravitational wave sources are usually expressed either in terms of cumulative density functions or in terms of *merger rate densities*. The merger rate densities represent the number of sources that merge in a comoving hypervolume and in a given parameter range. Given that the gravitational waves can be detected over different comoving hypervolumes depending on their frequency, chirp mass and detector sensitivity, the merger rate densities are the distribution functions that can better reproduce the intrinsic astrophysical ones.

Any distribution function is expressed in the form of a posterior probability and accounts for the many astrophysical and statistical limitations that affect the rough observed distributions. The corrections may enter as priors (like the intrinsic astrophysical population), likelihoods (like the signal-to-noise ratio that indicates the probability that each source is of astrophysical origin) or as normalization factors (like the correction for the sensible comoving hypervolume available for the detection, integrated for the observation time). In general, the observations are corrected for the limited sensitivity and detection efficiency but there is no extrapolation made to account also for the observational biases. [2]

Primary mass spectrum For each binary source, the primary mass is defined as the most massive one. Both the cumulative density function and the differential merger rate of the primary mass of the black hole binaries obtained at the end of the third observing run O3 are similar to the ones obtained at the end of the second observing run O2, as shown in Fig. 1.4. [6]

The differential merger rate of the primary mass observed at the end of O3 is a power-law with slope $\alpha = 3.5^{+0.6}_{-0.56}$ with a Gaussian peak centered in $M_{1,\mu} = 34^{+2.6}_{-4.0} \, M_\odot$. GWTC-3 hosts more low-mass system than GWTC-2, causing a steeper decline in the power law at higher masses and reducing the mass of the 99th percentile, now at $\sim 44 \, M_\odot$ and not at $\sim 60 \, M_\odot$ as it was in GWTC-2. There are strong overdensities at $\sim 10 \, M_\odot$ and $\sim 35 \, M_\odot$ that may reflect properties of the astrophysical environment but that are still under investigation.

Even though the region $\gtrsim 70 \, M_\odot$ is still weakly explored, there is no strong evidence for or
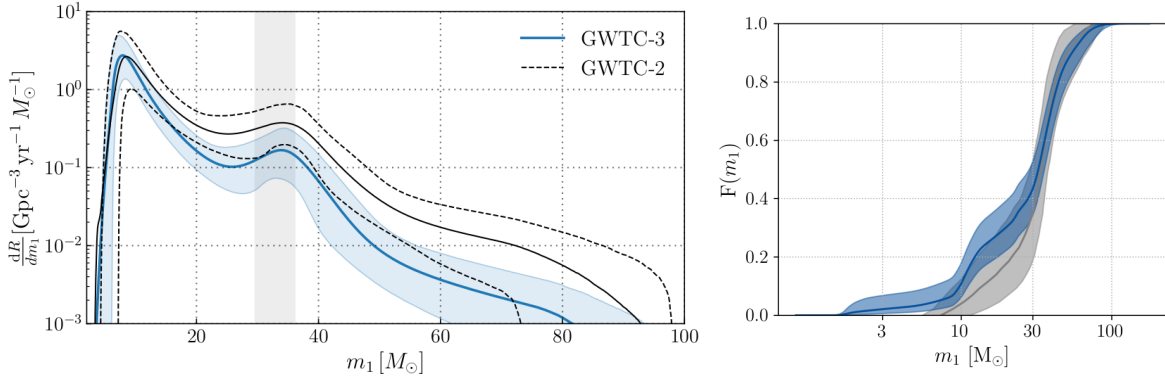
Figure 1.4: Differential merger rate (*left*) and cumulative density function (*right*) of the primary mass of the black hole binaries detected with the gravitational waves. In blue the posterior distributions obtained after the third observing run O3, in grey the ones obtained after O2. Thick solid lines denote the median values and are surrounded by the 90 % credible intervals. The vertical grey band on the differential merger rate indicates the 90 % credible interval for the mean of the Gaussian peak. [6]

against a mass-gap, at least up to $\sim 75\ M_\odot$. Still, a similar finding challenges the existence of the pair-instability mass gap from $\sim 60\ M_\odot$ to $\sim 120\ M_\odot$ [12]: either the single stellar evolution models need to be corrected (for instance, by lowering the triple-α reaction rate it is possible to shift to higher masses the lower boundary [13]) or black holes in that mass range (like the $\sim 69\ M_\odot$ and $\sim 95\ M_\odot$ black holes of GW190521 [14]) are not formed in the isolated binary scenario but, for instance, as the result of hierarchical merging in a dynamically active environment.[15] On the other hand, there is still evidence of a lower-mass gap between $\sim 3\ M_\odot$ and $\sim 5\ M_\odot$, potentially due to the physics of core-collapse supernovae and in agreement with the dearth of compact objects observed in the galactic X-ray binaries [16].

Spin distribution　On the one hand, the spin magnitude of the black holes in binary systems is expected to be influenced by the efficiency of the angular momentum transport in the stellar progenitors and by the binary processes like tides and mass transfer. On the other hand, the spin orientations are considered as proxy for the evolutionary channels: binary black holes formed from isolated binaries are expected to have spins aligned with their orbital angular momentum whereas dynamically assembled binaries have more likely isotropically oriented spins. Unfortunately, up-to-date it is still difficult to use the spins to discriminate between the different evolutionary scenarios for various reasons: they are difficult to constrain (they cause second-order effects in the gravitational waveform), their physical models are still rather poor (for instance the details on the angular momentum transport) and the core-collapse supernova may act as a random variable, further changing both the amplitude and the orientation of the spin. [6]

At the end of the third observing run, the black hole population exhibits a preference for low-spinning black holes $\chi \lesssim 0.4$, with a peak distribution at $\chi \sim 0.2$ and a large tail at higher values. Separate analysis of the fastest (χ_A) and slowest (χ_B) spinning components of the binary revealed that the rapid-spinning components are still quite slow $\chi_A \sim 0.4$ while the slow-spinning components are concentrated below $\chi_B \sim 0.2$, as expected. Posterior distributions for the spin magnitudes are shown in Fig. 1.5.

The effective spin parameter χ_{eff} distribution is a Gaussian centered in $\chi_{eff,\mu} = 0.06^{0.04}_{-0.05}$. The distribution peak is compatible with $\chi_{eff} = 0$, indicating spins misaligned with the orbital angular momentum. In particular, detailed analysis require the existence of negative effective spins $\chi_{eff} < 0$, related to polar angles $\theta \geq 90°$ and thus to black holes anti-aligned with the orbital angular momentum that likely formed in dynamically active environments. Moreover, data from GWTC-3 exhibit a mild anti-correlation between the effective spin parameter χ_{eff} and the mass ratio $q = M_2/M_1$, with $M_1 \geq M_2$. If confirmed, the anti-correlation would challenge the usual evolutionary pathaways for the binary black hole progenitors.
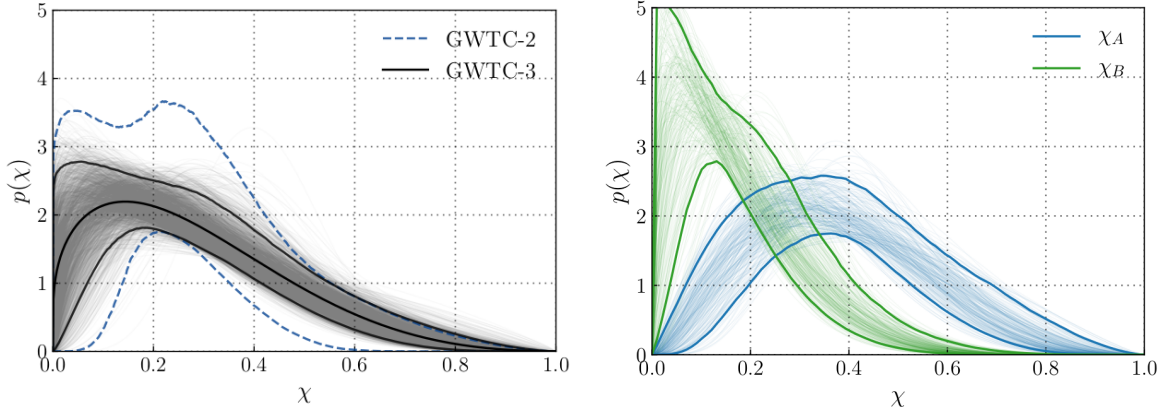
Figure 1.5: *Left:* Spin magnitudes posterior distribution of all the merging black holes at the end of the third observing run O3 (in gray) compared to the 90 % credible intervals for the sample limited at the end of O2 (in blue). *Right:* Separate posterior distributions within 90 % credible bounds of the fastest (χ_A, in blue) and slowest (χ_B, in green) black holes in the binaries. The new observations indicate a preference for slow-spinning black holes $\chi \lesssim 0.4$, with a fast-spinning component still rather slow $\chi_A \sim 0.4$ [6]
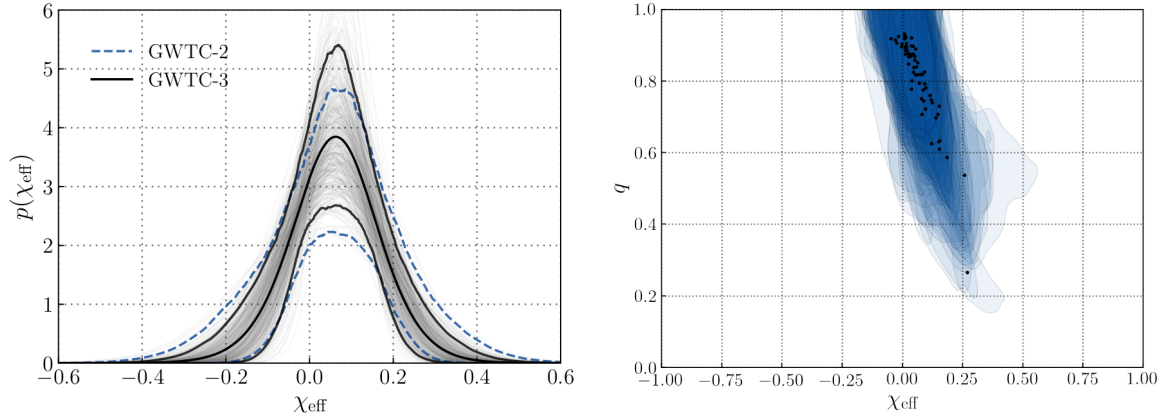

Figure 1.6: Spin magnitude (*left*) and misalignment with respect to the orbital angular momentum (*right*) of the merging black holes at the end of the third observing run O3 (in gray) compared to the 90 % credible intervals for the sample limited at the end of O2 (in blue). The new observations indicate a preference for low-spin magnitudes $\chi \lesssim 0.4$ and isotropically oriented spins. [6]
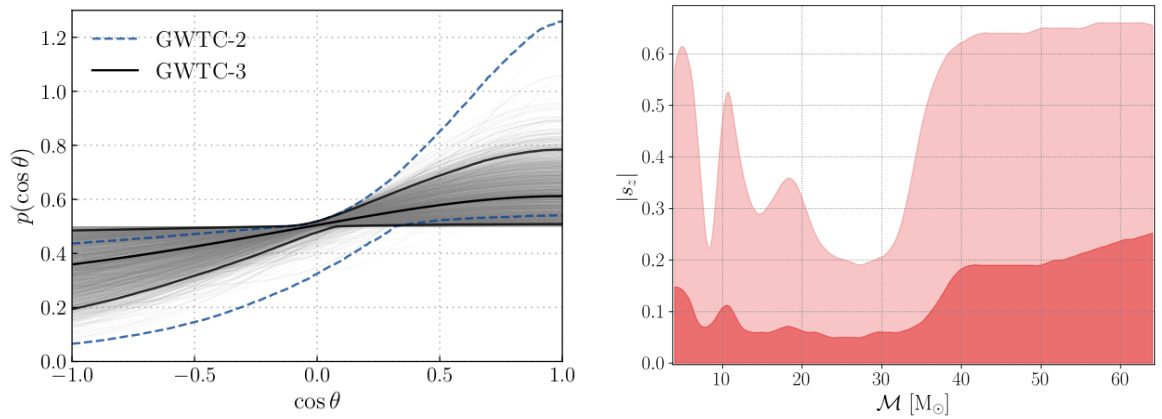
Figure 1.7: Differential merger rate (*left*) and cumulative density function (*right*) of the primary mass of the black hole binaries detected with the gravitational waves. In blue the posterior distributions obtained after the third observing run O3, in grey the ones obtained after O2. Thick solid lines denote the median values and are surrounded by the 90 % credible intervals. The vertical grey band on the differential merger rate indicates the 90 % credible interval for the mean of the Gaussian peak. [6]

1.2   Tensions in the binary black hole populations

The sources added in the GWTC-3 catalogue shed new light on the mass and spin distribution of the merging binary black holes [6].

[17, 18] analyzed the remnant properties of the GWTC-2 catalogue ([14]) and concluded that such systems could both evolve from isolated binaries in the galactic field and from dynamically active environments, such as young star clusters. The observations revealed merging BBHs with very different combinations of masses and spins, providing a precious sample to test and perfectionate the aformentioned models. In fact, in the first scenario, we expect that the evolution is dominated by binary processes like the Common Envelope (CE) and the Roche Lobe Overflow (RLO), that favour the sharing of mass and angular momentum between the two components and the production of remnants with aligned spins ([4]) and similar masses, up to $\sim 50\ M_\odot$ ([19]). In the second scenario we expect that hierarchical mergers and binary exchanges allow the formation of BHs in the pair-instability gap ($\sim 60 - 120\ M_\odot$), with mass ratios $q = M_2/M_1$ far from unity ([15]) and misaligned spins ([20]).

From an observational point of view, BBHs progenitors can be searched in binary systems that already contain a stellar BH. Nevertheless, BHs in quiescent systems are very difficult to observe with radial velocity ([21]) and astrometric measurements ([22]) and hopefully the new Gaia Data Releases will shade more light on them. On the contrary, BHs can be visible in the X-ray band if they are accreting mass from a companion star. These systems are called Black Hole X-Ray Binaries (BH-XRBs) and, according to [18], their progenitors share the same mass distribution of the progenitors of the primary BHs in the GWTC-2 catalogue (although the GW-BBHs progenitors exhibit slower spins, which leaves the debate open).

In this paper we will focus on the BH-XRBs systems made up by a Wolf-Rayet (WR) and a BH (hereafter, WR-BH systems) and we will try to constrain the conditions under which they could be progenitors of GW-BBHs systems in the isolated binary evolution scenario. We expect that these are very good candidates to form a GW-BBH, given that at solar metallicity $Z = Z_\odot = 0.02$ the WRs are formed from stars with initial mass $M_{\rm ZAMS} \gtrsim 30\ M_\odot$ ([23]), have strong line-driven winds and high mass loss rates $\dot{M} \sim 10^{-4} - 10^{-5}\ M_\odot/\mathrm{yr}$ ([24]). This means that WR stars are more likely to form a secondary BH in the neutrino-driven SuperNova (SN) scenario (threshold at $M_{\rm ZAMS} \gtrsim 25\ M_\odot$ for BH formation, [25]), and to produce a bright accretion disk around the primary BH ($L_{\rm X} \gtrsim 10^{36}$ erg/s, [26]).

Chapter 2

Theory and observations of Wolf-Rayet - black hole systems

2.1 Single stellar evolution to form a WR

Little recap of single stellar evolution on what is and how evolves a WR, underlying e.g. the typical progenitor masses and the importance of the stellar winds.

PLOT: SSE of 30 and 40 Msun with Z=0.015 and 0.02 to show influence of mass and stellar winds.

2.2 Mass transfer in binary systems

Short overview of the main binary processes, with particular attention to the wind accretion, Roche lobe overflow and common envelope

2.3 Observed candidates of Wolf-Rayet - black hole systems

The core is the paragraph I already wrote for the Computational Astrophysics exam (a table with the observed properties and short explanations on the uncertainties of the measurments). Brief review of the literature on possible evolutions of the systems as GW mergers.

2.4 Cyg X-3

Review of Koljonen+2017 and discussion on why values of Zdiarski+2013 are not reliable and we don't use them. Also describe it is in the MW and how we determined its metallicity and distance.

Host galaxy	Name	BH mass [$M_\odot$]	WR mass [$M_\odot$]	Period [h]	t_{GW} [Gyr]	Z [$Z_\odot$]
IC 10	IC10 X-1	23-33[a]	35[b]	34.9[a]	3.5	0.22
NGC 300	NGC300 X-1	13-21[d]	26[c]	32.8[d]	2.9	0.19
M101	M101 ULX-1	20-30	19	196.8	348	0.17
Milky Way	Cyg X-3	3	7	4.8	0.017	0.31
NGC 4490	CXOU J123030.3+413853	-	-	6.4	0.038	0.23
NGC 253	CXOU J004732.0-251722.1	-	-	14.5	0.33	0.24
Circinus	CG X-1	-	-	7.2	0.051	0.10

[a] [27]   [b] [28]   [c] [29]   [d] [30]

Table 2.1: Properties of the seven WR-BH candidates. The table is inspired by [31]. t_{GW} is an order-of-magnitude estimate calculated assuming $M_{1,BH} = M_{2,BH} = 10\ M_\odot$, given the uncertainties in the mass determination discussed in Section . The other parameters are extracted from the above referenced papers and from [32] (M101 ULX-1), [33] (Cyg X-3), [34] (CXOU J123030.3+413853), [35] (CXOU J004732.0-251722.1), [31] (CG-X1), [36] (Z).

2.4.1   Properties

Observations and identifications

Cyg X-3 lies in the galactic plane therefore no optical/UV counterpart has been detected yet due to interstellar absorption ([37]). Thus we know that the companion is a WR only by observing its IR spectrum. Using IR and X-ray emission lines, the companion is a low-mass BH or a NS.

DIstance and metallicity

McCollough2016 on the galactic plane ($l = 79.84°, b = +0.70°$). Distance 7.4 ± 1.1 kpc or, but less, probable, 10.2 ± 1.2 kpc. Distance estimated by looking at the "little friend" of Cyg X-3 i.e. a nearby Bok globule that was observed in X-ray by Chandra and then followed up with Submillimetric observations. This Bok globule is a 2-24 $M_\odot$gas+dust cloud confined in a 0.2 pc that scatters towards us the X-ray radiation produced in the nearby X-ray binary. Assuming that the velocity shift of the CO line is due only to the galactic rotation, the authors could use a tool for modeling the motion on the galactic disk and reconstructed a distance of 7.4 or 10.2 kpc (two values because of possible errors in the tool evaluation but the first is more probable).

We expect that Cyg X-3 was born in the star-forming region associated to the Bok globule and then the SN kick that formed the BH expelled the system from the Bok globule. Given that the binary is ~ 1 kpc away from the Bok globule and the lifetime of the WR, therefore the time elapsed from the SN, is $\sim 1-5 \times 10^6$ years, the authors estimate a SN kick of $\sim 190-980$ km/s, in agreement with some upper and lower independent constraints.

To model its metallicity we use the metallicty gradient of the MW that was obtained by **Lemasle2018** using Gaia data of metallicity and distance of 25 Cepheids. They found

$$[Fe/H] = -0.0447 * d_{\mathrm{Galacto}}(kpc) + 0.3522$$

. By tringulation, the galactocentric distance of Cyg X-3 is $d_{\mathrm{Galacto}} = 9.85$ kpc ($l = 79.84°$, heliocentric distance = 7.94 kpc from Lemasle 2018 and relative distance of Cyg X-3 = 7.4 kpc from the measurements on the BOk globule carried out by McCollough 2016). We therefore obtain

$$[Fe/H] = -0.088095$$

and, assuming that the metallicity distribution of the Sun is universal, we can convert such value to the metal mass fraction using

$$[Fe/H] = log(Z/X)_* - log(Z/X)_\odot$$

i.e. we obtain

$$Z_* = 0.91567 Z_\odot$$

. If we assume $Z_\odot$=0.02 we get $Z_* = 0.0183$ but if we assume $Z_\odot$=0.01524 we get $Z_* = 0.01395$.

2.4.2   Period

Singh 2002

4.8 hours. We take a larger range i.e. 4.5 - 5.1 hours, that combined with the possible mass ranges for WR and BH results in a semimajor of $a \sim 3 - 4$ Rsun

2.4.3   Mass ranges

Koljonen & Maccarone 2017

I used WR = 8 - 14 $M_\odot$, BH = 3. - 10 $M_\odot$

They derived: ??

Model: X-ray emission from compact object ionizes the stellar wind of the WR and causes the emission lines visible in the NIR (1-2.4 μm). They use a non-LTE model for the atmosphere of the

WR to reproduce the continuum + emission lines in the NIR.

Semimajor axis according to my model: Minimum possible a=3.052 Rsun with P=4.5 hours and Mtot = 8+3=11 $M_\odot$. Maximum possible a=4.303 Rsun with P=5.1 hours and Mtot = 14+10=24 $M_\odot$

Zdziarski 2013

[33] I used WR = 7.5 - 14.2 $M_\odot$, BH = 3 - 4.5 $M_\odot$

THey derived:WR = 7.5 - 14.2 $M_\odot$, Compact object = 1.3 - 4.5 $M_\odot$and then Belczynski 2012 assumed as MminBH = 2 $M_\odot$

Procedure

Vogliono risolvere un sistema a due variabili $\dot{M}$e MWR dove le due equazioni sono eq. 3 e eq 6 nel paper, che, combinate con altri dati osservativi e combinazioni, diventano le equazioni 7 e 8.

La prima descrive il rallentamento della binaria a causa del momento angolare trasportato via dal vento che lascia il sistema. Tale equazione lega Mdot, MWR+MCO, Pdot/P e di essa conosciamo $Pdot/P = 1.03 + -0.02x10^{-6}$ yr^{-1} da Kitamoto (comunicazione privata) e possiamo legare MCO alla massa della WR attraverso il mass ratio della binaria q che altro non è che il rapporto tra i due picchi delle due curve di rotazione

$$q = Mcompact/MWR = KWR/Kcompact \sim 0.23$$

Problema: Ko17 evidenziano che Zd13 hanno usato i dati di Hanson2000 che aveva usato come tracciante per il moto orbitale la linea di assorbimento HeI 2p-2s e che purtroppo è molto probabile che questa linea NON sia un tracciante per il moto orbitale bensì per il campo di velocità del vento della WR. Inoltre, lo spettro usato era stato preso nel 1999 durante un outburst, quando era presente anche una doppia linea di emissione He I 2p-2s a compilcare il tutto.

Semimajor axis according to my model: Minimum possible a=3.005 Rsun with P=4.5 hours and Mtot = 7.5+3=10.5 $M_\odot$. Maximum possible a=3.96 Rsun with P=5.1 hours and Mtot = 14.2+4.5=18.7 $M_\odot$

Chapter 3

Models and simulations with SEVN2

3.1 The SEVN2 population-synthesis code

Interpolates PARSEC tables, describe winds, criteria for identifying a WR, explain how, explain details of mass transfer, explain assumption on the pessimistic case, explain the three kick models, explain the three CCSN models (use histograms)
PLOT: histogram with compact remnants with different SN models
(PLOT: histogram with compact remnants with different kick models)

3.2 Initial conditions for simulations

Describe the distributions of masses, periods, eccentricities from which I derived the 1 million simulations. Scheme with the parameter space explored

Chapter 4

Results

4.1 > 90 % GW-BBH undergo WR-BH configuration

4 tabelle per i 4 modelli di kick che mostrano che nonostante si varino CCSN e metallicità è incontrovertibile che la WR-BH sia una configurazione obbligata.

4.2 Fiducial model

In dettaglio mostrare hist2d di a vs m1+m2 per progenitori, inizio WR-BH, remnants, m1+m2 vs tgw, m1 vs m2 progenitor, m1 vs m2 remnant.

In dettaglio analizzare evoluzione di Cyg X-3 con i trasferimenti di massa e le proprietà di osservabilità tipo il RL filling e la divisione in due/tre famiglie. Grafici: M1 VS M2, RL1fill vs RL2fill, RL1fill vs M1 per discutere il wind-fed, grafico periodo vs tempo in WR-BH per discutere tempo osservabilità, evoluzione di una singola binaria rappresentativa per tipo di mass transfer (RLO+RLO+CE, RLO +CE e CE+CE)

4.3 Role of metallicity

Comparare con stesso kick unified + 265 + CCSN = compact ma scegliendo Z=0.02 e discutere il diverso tempo evolutivo, canali e durata mass transfer e proprietà. Mostrare gli hist2d per a vs m1+m2 per progenitor e remnant e mostrare che sono gli stessi.

Poi usare come prima tre binarie rappresentative per i 3 tipi di mass transfer di Cyg X-3 e discutere le differenze rispeto a Z=0.15. Mostrare anche le differenze nei grafici M1 VS M2, RL1fill vs RL2fill.

4.4 Role of the kicks

Mostrare per Z=0.015 + CCSN= compact che diversi kicks cambiano principalmente il semiasse finale, scatterando molto di più i risultati delle GW-BBH ma lasciando quasi inalterati i candidati Cyg X-3 e la loro evoluzione. Mostrare i 4+4 grafici di a vs m1+m2 remnant e di m1vsm2 di Cyg X-3.

4.5 Role of CCSN model

Comparare prima con il kick fiducial unified+265 e Z=0.015 i tre modelli di CCSN e mostrare per ciascuno 2 grafici: M1 VS M2 per Cyg X-3 e a vs m1+m2 dei remnants. Ricordando le differeze iniziali nei modelli, spiegare le differenze.

4.6 Probing the parameter space

Mostrare a vs m1+m2 remnant e m1vsm2 Cyg X-3 a set di 3 CCSN variando i tre kick prima con Z=0.015 e poi con Z=0.02. Discutere come l'evoluzione di Cyg X-3 rimanga molto simile ma hobbs pure + rapid/delayed scatteri moltissimo le proprietà dei remnant

4.7 Compare with Belczynski+2013

??? Ha senso??

Chapter 5

Conclusion

- WR-BH as mandatory intermediate configuration needed to form GW-BBH at solar metallicity. Implication for spins (?)

- Well-defined properties for Cyg X-3 systems (say which), less defined for GW-BBH but quite well-constrained.

- At least a CE is needed + another CE or a stable RLO. Optional a third stable RLO for Cyg X-3 like systems. To be investigated if it is true also for GW-BBH but we think this may be representative for GW-BBH in the region of Cyg X-3

- CCSN introduces the most uncertainties in the masses of the remnants, thus selecting the evolutionary paths (e.g. the delayed almost completely removes the stable mass transfer channels)

- The kicks most favour the semimajor and when combined with rapid/delayed spread a lot the results

- Metallicity changes the stellar evolution and also spreads the results, even though a little less. Most importantly, it may transform the second mass transfer from RLO stable + CE into one single CE after a long RLO, all because the donor MS is able to expand/contract differently therefore R>RL long enough to become unstable before re-entering the RLO

Chapter 6

Annotazioni/Bozza

With the fiducial model i.e. Z=0.015, SN=compactness, kick=unified, sigma = 265

- Probability to form a WR/BH(cyg x-3 like) system in principle out of all binaries

- Probability to form a GW-BBH WR/BH(cyg x-3 like) system in principle out of all binaries

- Probability a WR-BH(cyg x-3 like) system has 2RLO/RLO+CE/2CE

- Probability it is visible in the WR-BH(cyg x-3 like) configuration?

- Time from system born, time from WRBH born, time to BHBH, time to merge all as a function of observed period and total mass

- probability it is observed as RL filling/wind fed system as function of semimajor

- evolutionary pathaway of WRBH (cyg x-3)

6.0.1 Parameter space to explore

OPtimistic o pessimistic scenario for RLO
Z= 0.02 and Z=0.015
SN = rapid, delayed, compact
Kicks = hobbs pure + sigma = 70 (Atri 2019, from median of 107 km/s)
Kicks = hobbs pure + sigma = 265
+ fiducial
+ Belczynski

6.0.2 Compare with Belczynski

Evolve with Z=0.02, SN=rapid, kick=sigma 265 + fallback as Fryer.

Belczynski considered Z=0.02 and sigma=265 always and always obtained a BBH. He varied different parameters though:

- rapid + hobbs + fallback = 14.2 WR + 4.5 BH –> 7.4 BH + 4.5 BH

- rapid + hobbs + fallback = 14.2 WR + 4.5 BH –> 8 BH + 4.5 BH (**NugisLamers2000 winds**)

- rapid + hobbs pure = 14.2 WR + 4.5 BH –> 7.4 BH + 4.5 BH

- delayed + hobbs + fallback = 14.2 WR + 4.5 BH –> 3.9 BH + 4.5 BH

Cioè con il rapid model, a prescindere dal kick model (=con o senza fallback) ottiene sempre che una WR di 14.2 iniziali diventa un BH di 7.4-8 Msun. Invece con il delayed (e il fallback) il BH è molto più leggero.

In ogni caso predicono che il sistema starà in configurazione WR-BH per 0.64 Myr

6.0.3   Notes on how SEVN works/how to interpret things/where to focus

Taglio della tesi:

- Primo aspetto/paper: per diventare GW-BBH a metallicità locale è NECESSARIO passare per la fase di WR-BH. Ammesso e non concesso (forte assunzione) che i GW-BBH osservati attualmente provengano da isolated channel a questa metallicità, ciò significa che gli spin devono essere gli stessi e questo sarebbe un grosso problema, visto che attualmente Vicky & Kalogera in apple e oranges hanno sottolineato che non è assolutamente la stessa cosa...

- Secondo aspetto/paper: cyg x-3 evolve così o colà a seconda del parameter space ma sembra avere proprietà iniziali/finali molto ben definite negli hist2D e ciò rende i risultati abbastanza well-constrained

- Per rendere questo risultato un po' più solido bisognerebbe anche esplorare le BH-NS, tutte le WR-BH che non sono cyg x-3, a metallicità più basse

Cosa non è chiaro/è da testare

- Kick = Unified + sigma = 70 km/s non ha senso perché unified è stato calibrato per riprodurre le osservazioni a partire dalla maxwelliana di hobbs. Pertanto è stato pensato per estrarre il kick da una maxwelliana di 265 km/s e poi diminuirne la magnitudine in base a ejecta e massa del remnant. Se parto già con una sigma di 70 sto già estraendo dei kick bassi, non posso diminuirli ancora di più...

- Il fatto che con hobbs puro io abbia un sacco di merging BBH ad alti semiassi posso provare a spiegarlo guardando all'eccentricità delle binarie, magari c'entra quanto vicine al periastro passano oppure no

- Overcontact binaries da testare perché passano quasi tutte per di là.Inoltre Giuliano spiega: questione overcontact binary: conosco bene questi casi e sono proprio alla base dell'ultima "importante" modifica di SEVN. Precedentemente questi casi andavano tutti a finire in merger o CE, ma ci siamo resi conto che in BSE/MOBSE questo check è disabilitato mentre c'è un RLO. Ora è cosi anche in SEVN. Ho già controllato che questi casi soprattutto durante un HG sono presenti anche in BSE/MOBSE.

  Quindi in sostanza ogni volta che il Raggio>RL e quindi c'è un RLO consideriamo per la stella un raggio effettivo pari a quello del RL per tutti i vari processi (venti,tides) mentre il Raggio della stella è usato solo per stimare il rate di mass transfer usando l'equazione 58 in Hurley02.

  Se questo sia il modo migliore per gestire il mass transfer non saprei, probabilmente no, ma si inserisce nel discorso piu ampio di andare oltre le prescriptions di Hurley. Abbiamo gia visto che lasciare che questi oggetti mergono in realtà è un assunzione che non funziona soprattuto considerando i merge rate delle neutron stars.

  Per fare un discorso pratico e concreto quello che ottieni in SEVN è consistente con Hurley e BSE/MOBSE ed è solo una conseguenza del modello di RLO adottato. Alla fine non ha nemmeno troppo senso avere plot in cui mostri il raggio durante il RLO perché per SEVN in questi casi il raggio effettivo della stella è pari a RL.

- la SN compact è descritta come nel paper della mapelli https://arxiv.org/pdf/2005.03055.pdf dove il grafico in basso è stato fittato con due distribuzioni. Se nel file .sh il parametro -1 è settato, allora la treshold zeta2.5 non è 0.3 come nel paper della mapelli ma viene estrapolata randomicamente da quelle distribuzioni (o una roba del genere). La SN= compactness è MOLTO biasata nel creare BH invece che NS

- per la SSE delle pure He posso confrontare la stessa stella se tipo mi faccio printare anche la colonna "zams" che mi dice qual è la traccia che sta usando per l'interpolazione (a seconda della tabella usata)

- Capire nel dettaglio le differenze tra Z=0.02 e Z=0.015

- Focus sul final fate dopo la WR-BH per un confronto con Belczynski

- controllare le incertezze sulle masse di KO17!!! Specialmente la metallicità usata per la M WR dalla relazione M-L

- Pessimistic/optimistic case riguarda la possibilità che una stella in HG possa entrare ed eventualmente sopravvivere ad un CE (optimistic) oppure si fonda direttamente con la compagna nell'ipotesi di assenza di un core ben definito (pessimistic)

They predict:

- WR progenitor of 50 Msun produces WR of 14.2 Msun with R=1.2 Rsun and Rlobe = 1.8 in a=3.8 Rsun orbit with a BH of 4.5 Msn as companion

- mass loss rates for the WR taken from Hurley 2000 + Hamann & Koesterke 1998 (theoretical)

$$\dot{M} = 10^{-13}(L/L_\odot)^{1.5} M_\odot \mathrm{yr}^{-1}$$

- WR lives for 0.64 Myr and becomes a 8.2 Msun WR with CO core of 6.2 Msun and orbit expanded to a=5.6 Rsun.

- rapid core collapse for the WR leads to fallback=1 but with the 10% of the gravitational mass lost due to neutrinos we obtain a secondary BH of 7.4 Msun with NO NATAL KICK (because the fallback is maximum therefore it is fully damped), slightly wider orbit of a=6 Rsun and e=0.07.

- the final BHBH of 7.4 Msun + 4.5 Msun has a chirp mass of 5.0 Msun and will merge in 500 Myr.

Different wind:

- Use wind taken from Nugis & Lamers 2000 as done in Zdziarski i.e. by selecting the ones for WR stars with the desired masses (empirical based on 64 WR in the MW. In particular in the mass range I am interested, out of the 34 observed WR, 19 were mostly in a binary system)

$$\dot{M} = 1.9 \times 10^{-5}(M_{WR}/14.7 M_\odot)^{2.93} M_\odot \mathrm{yr}^{-1}$$

- Slight increase in the BH formed after the WR (8 Msun instead of the previous 7.4 Msun. Probably because they are lower than the theoretical ones so they retain more mass i.e. they form a heavier BH in the end).

- No other appreciable changes

Different kick:

- if no fallback the probabilty to form a merging BHBH system reduces from 100% sure to only 68% because some systems are disrupted by the larger kicks

Different SN:

- delayed model forms a lighter BH (3.9 Msun instead of the 7.4 Msun) because the delayed explosion allows more mass to escape and not to accrete back. This also lowers the formation efficiency to 50%

6.1 Compactness model implemented in SEVN

As explained in Mapelli+2020 [38], the compactness model in SEVN uses the final CO mass to interpolate the compatness parameter

$$\xi_{2.5} = 0.55 - 1.1 \left(\frac{1 M_\odot}{m_{\mathrm{CO}}} \right) \tag{6.1}$$

where the above formula is derived with fits to FRANEC data.

Patton and Sukhbold 2020 [39], in the bottom figure of Fig. 3, provide the probability that a star with a given compactness parameter undergoes an explosion or implosion. We fitted to that data a probability distribution and use it to randomly decide whether out star with that compactness will explode, forming a NS, or will implode, forming a BH.

After the compact remnant is formed,

6.2 Pipeline

- Su demoblack result.py, read.py e WRBH.py per generare i file WRBH, BHBH, BHNS, result.txt e le cartelle dataframes e copied. Il tutto viene salvato in una cartella che identifica la simulazione e si chiama tipo 1mln_Z015_com_unified265

- Quest'analisi include nei file WRBH, BHBH e BHNS tutti i corrispondenti candidati usando come criterio di classificazione unicamente la PhaseBSE e NON la massa

- La cartella tipo 1mln_Z015_com_unified265 viene copiata sul pc

- Si fa debugging per estrarre correttamente i BH, cioè scegliendo se considerare come "veri" BH anche i BH con massa < 3 che si originano dalla PPISN. Per fare ciò si fanno andare gli script result2.py, read2.py e WRBH2.py scegliendo, a seconda, l'opzione desiderata per il debugging: debug= 'ppisn' sceglie come massa minima per i BH in Cyg X-3 quella pari a ?? in base a ?? mentre l'opzione debug='real' seleziona come BHBH e BHNS solo i sistemi dove il BH sia un oggetto compatto con massa > 3

6.3 Results Cyg X-3

Present results with different parameters (SN model and metallicity) and show how they impact on the evolution in general. Underline the main evolutionary paths (RLO/CE) and progenitors and remnant properties (like the computational exam)

Then show detailed evolution for Cyg X-3 only, showing differences with Belczynski 2013.

Bibliography

[1]   B. P. Abbott et al. "Observation of Gravitational Waves from a Binary Black Hole Merger".
       In: *Physical Review Letters* 116.6, 061102 (Feb. 2016), p. 061102. DOI: 10.1103/PhysRevLett.
       116.061102.

[2]   The LIGO Scientific Collaboration et al. "GWTC-3: Compact Binary Coalescences Observed
       by LIGO and Virgo During the Second Part of the Third Observing Run". In: *arXiv e-prints*
       (Nov. 2021), arXiv:2111.03606.

[3]   Nicola Giacobbo et al. "The progenitors of compact-object binaries: impact of metallicity, com-
       mon envelope and natal kicks". In: *Monthly Notices of the Royal Astronomical Society* 480.2
       (Oct. 2018), pp. 2011–2030. DOI: 10.1093/mnras/sty1999.

[4]   Vassiliki Kalogera. "Spin-Orbit Misalignment in Close Binaries with Two Compact Objects".
       In: *Astrophysical Journal* 541.1 (Sept. 2000), pp. 319–328. DOI: 10.1086/309400.

[5]   BP Abbott et al. "GWTC-1: a gravitational-wave transient catalog of compact binary mergers
       observed by LIGO and Virgo during the first and second observing runs". In: *Physical Review
       X* 9.3 (2019), p. 031040.

[6]   LIGO Scientific Collaboration et al. "The population of merging compact binaries inferred using
       gravitational waves through GWTC-3". In: *arXiv preprint arXiv:2111.03634* (2021).

[7]   Michele Maggiore. *Gravitational waves: Volume 1: Theory and experiments*. OUP Oxford, 2007.

[8]   Maurizio Spurio. "An introduction to astrophysical observables in gravitational wave detec-
       tions". In: *arXiv preprint arXiv:1906.03643* (2019).

[9]   BP Abbott et al. "A gravitational-wave measurement of the Hubble constant following the
       second observing run of Advanced LIGO and Virgo". In: *The Astrophysical Journal* 909.2 (2021),
       p. 218.

[10]   Bangalore Sathyaprakash et al. "Cosmology and the early universe". In: *Bulletin of the AAS*
       51.3, 248 (May 2019), p. 248.

[11]   Feryal Ozel et al. "Masses, Radii, and the Equation of State of Neutron Stars". In: *Annual
       Review of Astronomy and Astrophysics* 54 (Sept. 2016), pp. 401–440. DOI: 10.1146/annurev-
       astro-081915-023322.

[12]   Mario Spera et al. "Very massive stars, pair-instability supernovae and intermediate-mass black
       holes with the sevn code". In: *Monthly Notices of the Royal Astronomical Society* 470.4 (Oct.
       2017), pp. 4739–4749. DOI: 10.1093/mnras/stx1576.

[13]   Guglielmo Costa et al. "Formation of GW190521 from stellar evolution: the impact of the
       hydrogen-rich envelope, dredge-up, and ^{12}C$(\alpha, \gamma)^{16}$O rate on the pair-instability black hole
       mass gap". In: *Monthly Notices of the Royal Astronomical Society* 501.3 (Mar. 2021), pp. 4514–
       4533. DOI: 10.1093/mnras/staa3916.

[14]   R. Abbott et al. "GWTC-2: Compact Binary Coalescences Observed by LIGO and Virgo during
       the First Half of the Third Observing Run". In: *Physical Review X* 11.2, 021053 (Apr. 2021),
       p. 021053. DOI: 10.1103/PhysRevX.11.021053.

[15]   Sara Rastello et al. "Dynamics of binary black holes in low-mass young star clusters". In:
       Monthly Notices of the Royal Astronomical Society 507.3 (Nov. 2021), pp. 3612–3625. DOI:
       10.1093/mnras/stab2355.

[16]   Feryal Özel et al. "The black hole mass distribution in the galaxy". In: *The Astrophysical Journal*
       725.2 (2010), p. 1918.

[17] R. Abbott et al. "Population Properties of Compact Objects from the Second LIGO-Virgo Gravitational-Wave Transient Catalog". In: *Astrophysical Journal, Letters* 913.1, L7 (May 2021), p. L7. DOI: 10.3847/2041-8213/abe949.

[18] Maya Fishbach et al. "Apples and Oranges: Comparing black holes in X-ray binaries and gravitational-wave sources". In: *The Astrophysical Journal Letters* 929.2 (2022), p. L26.

[19] Nicola Giacobbo et al. "Merging black hole binaries: the effects of progenitor's metallicity, mass-loss rate and Eddington factor". In: *Monthly Notices of the Royal Astronomical Society* 474.3 (Mar. 2018), pp. 2959–2974. DOI: 10.1093/mnras/stx2933.

[20] Carl L. Rodriguez et al. "Illuminating Black Hole Binary Formation Channels with Spins in Advanced LIGO". In: *Astrophysical Journal, Letters* 832.1, L2 (Nov. 2016), p. L2. DOI: 10.3847/2041-8205/832/1/L2.

[21] Todd A. Thompson et al. "A noninteracting low-mass black hole-giant star binary system". In: *Science* 366.6465 (2019), pp. 637–640. DOI: 10.1126/science.aau4005.

[22] Łukasz Wyrzykowski et al. "Constraining the masses of microlensing black holes and the mass gap with Gaia DR2". In: *Astronomy and Astrophysics* 636, A20 (Apr. 2020), A20. DOI: 10.1051/0004-6361/201935842.

[23] Marco Limongi et al. "Presupernova evolution and explosion of massive stars". In: *Journal of Physics Conference Series*. Vol. 202. Journal of Physics Conference Series. Jan. 2010, p. 012002. DOI: 10.1088/1742-6596/202/1/012002.

[24] G. Gräfener et al. "Mass loss from late-type WN stars and its Z-dependence. Very massive stars approaching the Eddington limit". In: *Astronomy and Astrophysics* 482.3 (May 2008), pp. 945–960. DOI: 10.1051/0004-6361:20066176.

[25] Tuguldur Sukhbold et al. "Core-collapse Supernovae from 9 to 120 Solar Masses Based on Neutrino-powered Explosions". In: *Astrophysical Journal* 821.1, 38 (Apr. 2016), p. 38. DOI: 10.3847/0004-637X/821/1/38.

[26] A. V. Tutukov et al. "Wolf-Rayet stars with relativistic companions". In: *Astronomy Reports* 57.9 (Sept. 2013), pp. 657–668. DOI: 10.1134/S1063772913090084.

[27] Jeffrey M. Silverman et al. "On IC 10 X-1, the Most Massive Known Stellar-Mass Black Hole". In: *The Astrophysical Journal* 678.1 (Apr. 2008), pp. L17–L20. DOI: 10.1086/588096.

[28] J. S. Clark et al. "On the Wolf-Rayet counterpart to IC 10 X-1". In: *Astronomy and Astrophysics* 414 (Jan. 2004), pp. L45–L48. DOI: 10.1051/0004-6361:20031762.

[29] P. A. Crowther et al. "NGC 300 X-1 is a Wolf-Rayet/black hole binary". In: *Monthly Notices of the Royal Astronomical Society: Letters* 403.1 (Mar. 2010), pp. L41–L45. ISSN: 1745-3925. DOI: 10.1111/j.1745-3933.2010.00811.x.

[30] Breanna A Binder et al. "The Wolf–Rayet+ Black Hole Binary NGC 300 X-1: What is the Mass of the Black Hole?" In: *The Astrophysical Journal* 910.1 (2021), p. 74.

[31] P. Esposito et al. "Periodic signals from the Circinus region: two new cataclysmic variables and the ultraluminous X-ray source candidate GC X-1". In: *Monthly Notices of the Royal Astronomical Society* 452.2 (Sept. 2015), pp. 1112–1127. DOI: 10.1093/mnras/stv1379.

[32] Ji-Feng Liu et al. "Puzzling accretion onto a black hole in the ultraluminous X-ray source M 101 ULX-1". In: *Nature* 503.7477 (Nov. 2013), pp. 500–503. DOI: 10.1038/nature12762.

[33] A. A. Zdziarski et al. "Cyg X-3: a low-mass black hole or a neutron star." In: *Monthly Notices of the Royal Astronomical Society* 429 (Feb. 2013), pp. L104–L108. DOI: 10.1093/mnrasl/sls035.

[34] P. Esposito et al. "Discovery of a 6.4 h black hole binary in NGC 4490". In: *Monthly Notices of the Royal Astronomical Society* 436.4 (Oct. 2013), pp. 3380–3387. ISSN: 0035-8711. DOI: 10.1093/mnras/stt1819.

[35] Thomas J. Maccarone et al. "A new candidate Wolf-Rayet X-ray binary in NGC 253". In: *Monthly Notices of the Royal Astronomical Society* 439.3 (Apr. 2014), pp. 3064–3072. DOI: 10.1093/mnras/stu167.

[36] M Mapelli et al. "Ultra-luminous X-ray sources and remnants of massive metal-poor stars". In: *Monthly Notices of the Royal Astronomical Society* 408.1 (2010), pp. 234–253.

[37] K. I. I. Koljonen et al. "Gemini/GNIRS infrared spectroscopy of the Wolf-Rayet stellar wind in Cygnus X-3". In: *Monthly Notices of the Royal Astronomical Society* 472.2 (Dec. 2017), pp. 2181–2195. DOI: 10.1093/mnras/stx2106.

[38] Michela Mapelli et al. "Impact of the Rotation and Compactness of Progenitors on the Mass of Black Holes". In: *Astrophysical Journal* 888.2, 76 (Jan. 2020), p. 76. DOI: 10.3847/1538-4357/ab584d.

[39] Rachel A. Patton et al. "Towards a realistic explosion landscape for binary population synthesis". In: *Monthly Notices of the Royal Astronomical Society* 499.2 (Dec. 2020), pp. 2803–2816. DOI: 10.1093/mnras/staa3029.